

Investigations of Propulsion Integration Interference Effects on a Transport Aircraft Configuration

C.-C. Rossow*

DLR, Institut für Entwurfsaerodynamik, D-38108, Braunschweig, Germany

J.-L. Godard†

ONERA, F-92322 Chatillon, France

H. Hoheisel‡

DLR, Institut für Entwurfsaerodynamik, D-38108, Braunschweig, Germany

and

V. Schmitt§

ONERA, F-92322 Chatillon, France

In a joint effort ONERA and DLR have assessed the interference effects of a generic twin-engine transport aircraft configuration equipped with throughflow nacelles. Both experimental and theoretical investigations were performed. The results showed that the installation of the nacelles had substantial effects on total forces at cruise Mach number. With respect to the clean configuration, total lift decreased at constant incidence, and total drag increased at constant lift. A detailed analysis of the flowfield revealed that for transonic flows the installation of the nacelle influenced the complete upper wing surface. On the lower wing surface the flow was considerably accelerated due to the propulsion system, and a supersonic region terminated by a shock wave appeared. The nacelle pressure distribution was also substantially influenced by interference effects. Comparison of experimental and numerical results showed that the solution of the Euler equations is well capable of simulating the interference effects.

Introduction

ENGINE/AIRFRAME integration is a key feature in the design and development of advanced technology aircraft,^{1,2} and it is clear that it is highly dependent on power-plant developments. It has been stated that the propulsive efficiency of state-of-the-art turbofans still has a large potential of improvement through significant increases of the bypass ratio (perhaps from 5 up to 15).³ Other propulsive concepts are, of course, open rotors or high-speed propellers (UDF, Propfan). All these concepts offer potential fuel savings of up to 30% in comparison to current fan engines, but they will have strong effects on propulsion/airframe integration and even on aircraft configuration.

In order to deal with these challenges, there is an urgent need to improve the understanding of the engine/airframe interference mechanisms through careful analysis of local flow behavior by means of wind-tunnel testing. There is also the need to develop and validate computational tools aimed at the prediction of interference effects caused by propulsion/airframe integration.

During the last couple of years, both DLR and ONERA have been working on these topics.^{4,5} In addition, some activities based on a generic transport aircraft configuration have been undertaken together. The propulsion units of this configuration were represented by throughflow nacelles, for

which strong interference effects were anticipated. In a first step experimental investigations of this configuration were carried out in one of the major European test facilities, the S2MA wind tunnel of the ONERA test center in Modane. After these tests, computations on the same configuration were performed by DLR using the CEVCATS code for the solution of the Euler equations. The aim of this article is to report on the progress of this work.

Experimental and Theoretical Approaches

Generic Transport Aircraft Configuration

The configuration considered in this study is a twin-engine aircraft that represents a typical modern wide-body transport aircraft of Airbus-type. The geometry is a wing-body configuration derived from the DLR-F4 configuration.⁶

The design Mach number of the wing is $M_\infty = 0.785$ at a lift coefficient of $C_L = 0.5$. The main geometrical data of the wing are the following:

Aspect ratio Λ	= 9.5
Taper ratio λ	= 0.3
Leading-edge sweep φ	= 27.1 deg
Quarterchord sweep φ_{25}	= 25.0 deg
Dihedral φ_D	= 4.8 deg

The shape of the fuselage is defined by a forebody, including a cockpit, a cylindrical part containing the wing, and an afterbody. The propulsion units were simulated by throughflow nacelles. The nacelles are axisymmetric with nacelle lines derived from CFM56-5 nacelles in a long duct version, and the fan diameter is the same as in the three-dimensional nacelle to achieve a realistic mass flow coefficient of $\varepsilon = 0.71$. The chosen nacelle location gives rise to quite strong interference effects, and the pylon is of symmetrical shape.

In the following the specific model described above will be called the DLR-F6 configuration. Figure 1 presents a view of the model in tailoff configuration including the main geometrical dimensions.

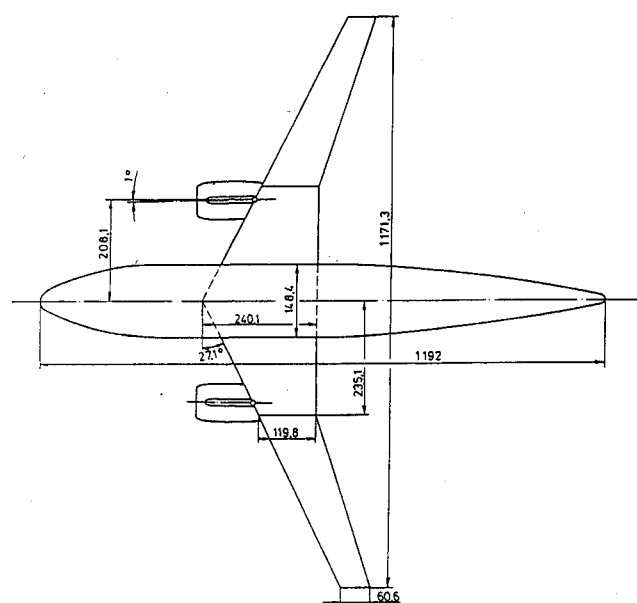
Presented as Paper 92-3097 at the AIAA 28th Joint Propulsion Conference and Exhibit, Nashville, TN, July 6–8, 1992; received Oct. 29, 1992; revision received Oct. 1, 1993; accepted for publication Oct. 11, 1993. Copyright © 1992 by the American Institute of Aeronautics and Astronautics, Inc. All rights reserved.

*Research Scientist, Propulsion Integration. Member AIAA.

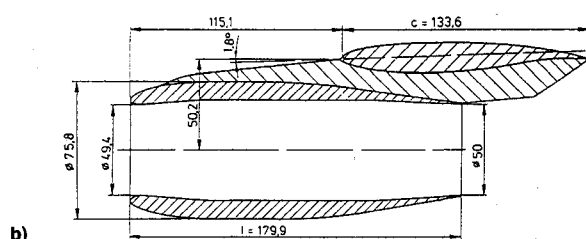
†Research Engineer, Applied Aerodynamics, Direction de l'Aerodynamique, BP 72.

‡Head, Propulsion Integration.

§Head, Propulsion Integration, Direction de l'Aerodynamique, BP 72.



a) wing reference area $S = 0.1453\text{m}^2$
aerodynamic mean chord $c = 0.1412\text{m}$



b) throughflow nacelle.

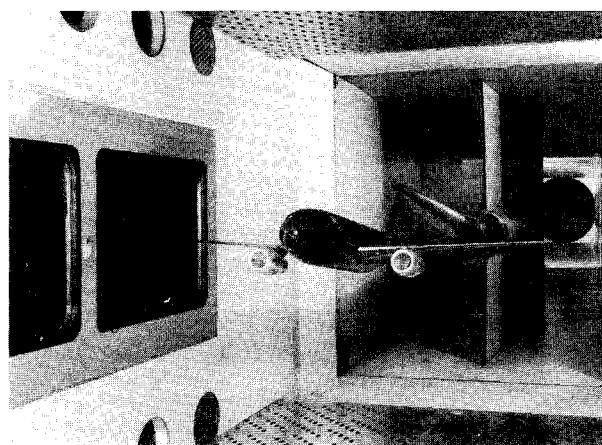


Fig. 2 ONERA S2MA wind tunnel with DLR-F6 configuration.

Experimental Approach

Test Setup

The experiments using the DLR-F6 wind-tunnel model were performed in the S2MA pressurized wind tunnel of the ONERA center in Modane.⁷ The transonic test section has a height of 1.77 m and a width of 1.75 m. In order to reduce wall influence it has perforated top and bottom walls.

Since very precise drag determination is required, the model is mounted by a fin sting through a six-component balance for overall force and moment measurements. Figure 2 shows

the generic transport aircraft model in the test section of the S2MA wind tunnel.

For detailed analysis of the flow, the model is instrumented with 344 static pressure taps, with 288 pressure taps located in 8 spanwise sections of the wing. The nacelle is equipped with 47 pressure holes in 3 equally spaced radial sections at 60, 180, and 300 deg.

Measurements

Tests were carried out for the following configurations: 1) wing-body (WB), and 2) wing-body-pylon-nacelle (WBPB).

The tests cover a Mach number range

$$0.3 < M_\infty < 0.82$$

as well as sweeps of incidence α , corresponding to the range of lift coefficient

$$0.0 < C_L < 0.6$$

at various Mach numbers.

The Reynolds number is kept constant, equal to 3×10^6 , by control of the total pressure. The transition is fixed on the fuselage, the wing, and the nacelles by transition strips.

Total forces and moments are measured continuously during α sweeps at a fixed Mach number. Pressure distributions are measured on all components of the model at fixed Mach number and incidence.

All force and moment data are corrected in the usual way, including wall corrections and model support corrections. Overall force and moment measurement repeatability has been checked for the cruise Mach number $M_\infty = 0.75$. It appears that the scatter of the drag coefficient is less than $\Delta C_D = \pm 0.6 \times 10^{-4}$.

Theoretical Approach

Besides experimental investigations, the analysis of interference effects is performed by numerically solving the Euler equations.

Solution Scheme

The solution scheme applied is the DLR-code CEVCATS. The code requires body-fitted structured meshes. The discretization is performed using a central differencing cell-vertex finite volume scheme with artificial dissipation. For time integration an explicit Runge-Kutta scheme is employed, and convergence towards steady state is accelerated using local time stepping, implicit residual averaging, and multigrid. The code is written in a block-structured form and allows an arbitrary application of boundary conditions on the block faces. Details of the code structure may be found in Ref. 8.

Grid Generation

For the CEVCATS code, body-fitted block-structured meshes have to be generated. Using the grid generation concept of Ref. 9, a H-type grid structure in streamwise direction and an O-type structure in spanwise direction is employed for the wing-body combination. Nacelle and pylon are integrated into this basic grid by introducing a subblock containing these components. A three-dimensional view of the field grid around the F6 configuration with nacelles is shown in Fig. 3. The complete field grid for the WBPB configuration consists of 10 computational blocks with about 650,000 mesh points in total.

Capabilities and Limits of the Theoretical Approach

Using the solution of the Euler equations, viscous effects are neglected. This causes more or less distinct and systematic deviations between experimental and computational results. This is especially true for the inviscid simulation of the transonic flow around a lifting wing with significant rear-loading.

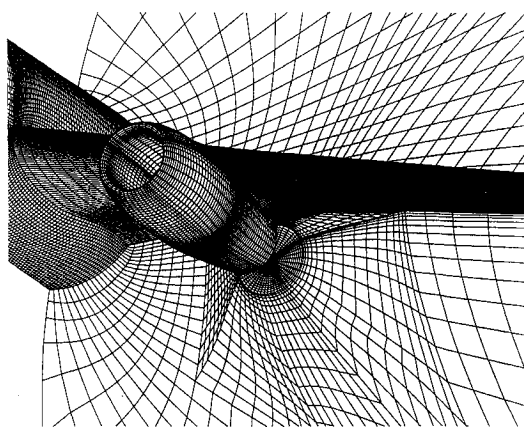


Fig. 3 Field grid.

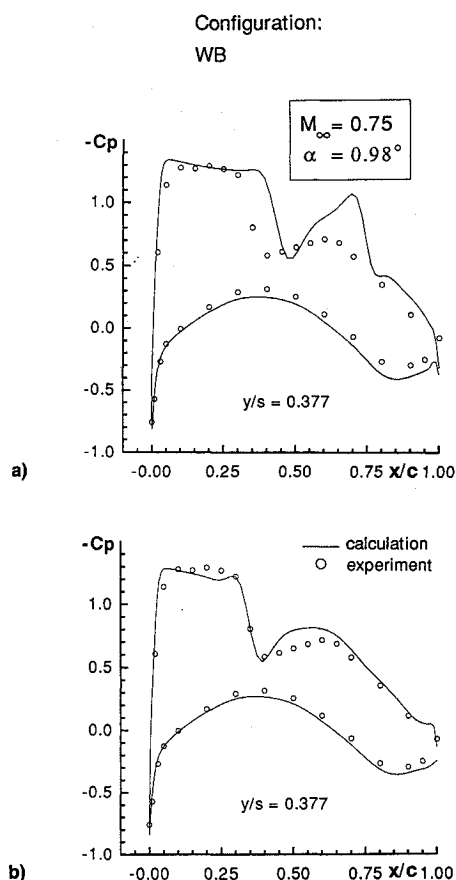


Fig. 4 Wing pressure distribution with and without displacement thickness: a) solution of Euler equations and b) solution of Euler equations with added displacement thickness.

Figure 4a shows a comparison of the experimental and computational pressure distribution for the F6 wing-body combination at a spanwise location of $\eta = 0.377$. The computational results were obtained by the solution of the Euler equations with the CEVCATS code. The figure shows the following: first, the shock is predicted too far downstream. Second, in the computation a second shock arises, which is not observed in the experiment. Third, the effect of the rear-loading is overpredicted by the inviscid simulation. These effects will lead to an overprediction of local and total lift forces.

Figure 4b shows the pressure distribution for the same configuration, but in this case viscous effects have been taken into account by adding the displacement thickness onto the wing geometry. The displacement thickness has been calculated in advance by using a boundary-layer code coupled with

a potential flow code.¹⁰ The calculated shock position now agrees well with the experiment. The displacement thickness of the boundary layer causes a decambering of the airfoil, and thus the shock is moved upstream. Additionally, the secondary shock has vanished, although pressure is still somewhat underpredicted in the region aft of the shock. On the lower surface, the overprediction of the rear-loading has been reduced compared to the pure solution of the Euler equations. Since the adverse pressure gradient in the rear-loading region causes a thickening of the boundary layer, this tends to compensate the camber in the aft portion of the airfoil.

It is important to bear in mind these limitations in the following. In this study the capability to predict interference effects is of interest, and this should not be confused with the a priori known limitations of the theoretical method.

Results

Global Interference Effects

In this section the overall effects of the propulsion integration on total forces are described, in particular lift and drag as deduced from the experiments.

Lift and Drag Coefficient

The installation of nacelles leads to a decrease of lift, illustrated by $C_L(\alpha)$ curves at a Mach number of $M_\infty = 0.75$ (Fig. 5a). For the cruise condition ($M_\infty = 0.75$, $C_L = 0.5$), it is necessary to increase the incidence of the WBPN configuration by 0.5 deg to obtain the same lift as for the WB configuration. The difference in lift coefficient between both configurations is $\Delta C_L = 0.06$ (12%).

The development of lift vs incidence is almost linear for the WB configuration. At a given incidence, the loss of lift due to the nacelles is nearly constant for a range of α from approximately $-1 < \alpha < 2$ deg. For lower incidences, the difference in lift vanishes.

Assuming that nacelle and pylon have a negligible contribution to the total lift, the loss of lift may be explained by modifications of the flowfield on the wing due to the nacelle and pylon interference.

The polars $C_L(C_D)$ show an important increase of drag due to the presence of nacelles for the cruise Mach number $M_\infty = 0.75$ (Fig. 5b). For the cruise lift $C_L = 0.5$, the additional amount of drag is $\Delta C_D = 42 \times 10^{-4}$ (+14%). The minimum value of drag for the WBPN configuration is obtained at a higher lift than for the WB configuration. This indicates a stronger interference effect of the nacelles on drag for low lift coefficients.

The variation of drag with Mach number at cruise lift $C_L = 0.5$ is also different for both configurations (Fig. 5c). In addition to the general increase of drag due to the propulsion units, the slope of the curve $C_D(\text{Mach})$ is steeper for the WBPN configuration. The reduction in the drag rise Mach number for the WBPN configuration is probably caused by the appearance of shock waves on the lower surface of the wing, in the region of nacelle and pylon, for higher Mach numbers.

Installation Drag

In the case of transport aircraft studies, an important parameter for the performance analysis is the installation drag coefficient $C_{D_{\text{inst}}}$. This coefficient is defined by

$$C_{D_{\text{inst}}} = C_{D(\text{complete model})} - C_{D(\text{clean wing})} - C_{D(\text{nacelles internal drag})}$$

The internal drag of the nacelles is deduced from special calibration tests. It has to be subtracted because it does not belong to the drag balance in the thrust and drag accounting procedure.

Therefore, the drag increment due to the propulsion units $C_{D_{\text{inst}}}$ includes the external drag of the nacelles, the drag of

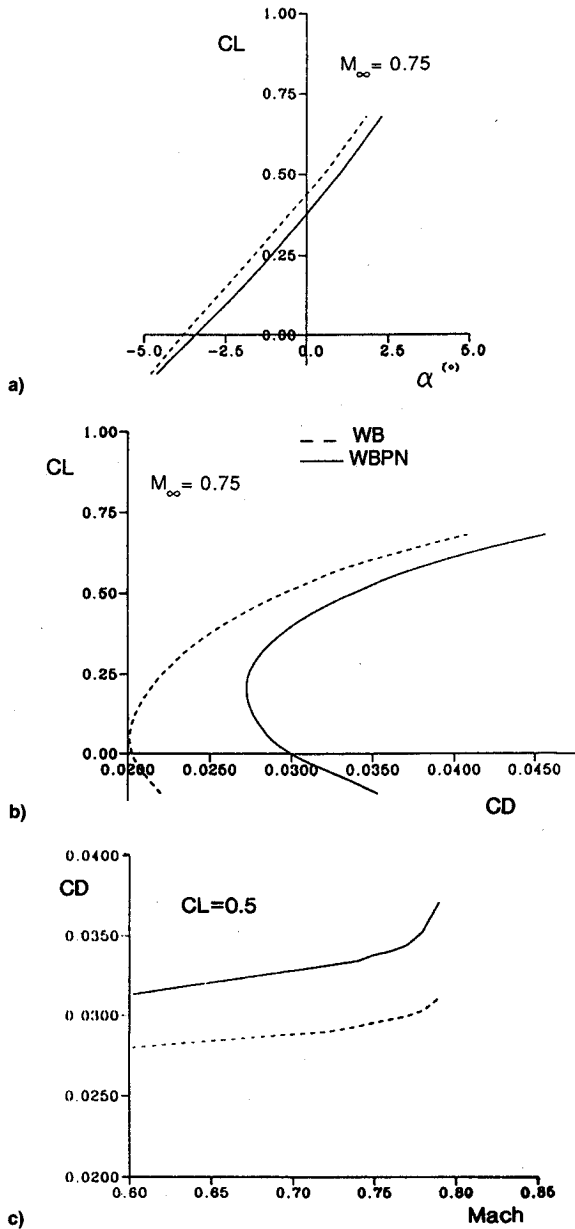


Fig. 5 Total force measurements with and without nacelles: a) lift coefficient, b) drag coefficient, and c) drag at cruise lift.

the pylons, and the interference drag. The interference drag, which represents the drag difference between assembled and isolated components (wing, pylon, and nacelle), must not be confused with $C_{D_{inst}}$.

The $C_L(C_{D_{inst}})$ curve for the cruise Mach number (Fig. 6) shows that $C_{D_{inst}}$ is almost constant, at a value close to 30×10^{-4} , for values of C_L from $0.3 < C_L < 0.7$. For lower lift coefficients, it increases drastically. As will be discussed later this may be explained by the appearance of shock waves or local separations on the lower wing surface inboard of the nacelle installation. As the same figure illustrates, at a lower Mach number of $M_\infty = 0.6$, $C_{D_{inst}}$ has a much weaker evolution at low C_L .

Detailed Analysis of Interference Effects

In this section a more detailed analysis of the interference effects based on the surface pressure distributions will be made. Both experimental and computational results will be used. In order to limit the amount of data to be presented, the investigations are focused on transonic flow at the cruise Mach number $M_\infty = 0.75$ and $\alpha = 0.98$ deg, which corre-

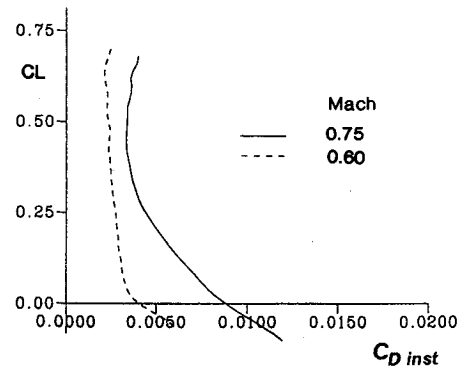


Fig. 6 Variation of installation drag with lift coefficient.

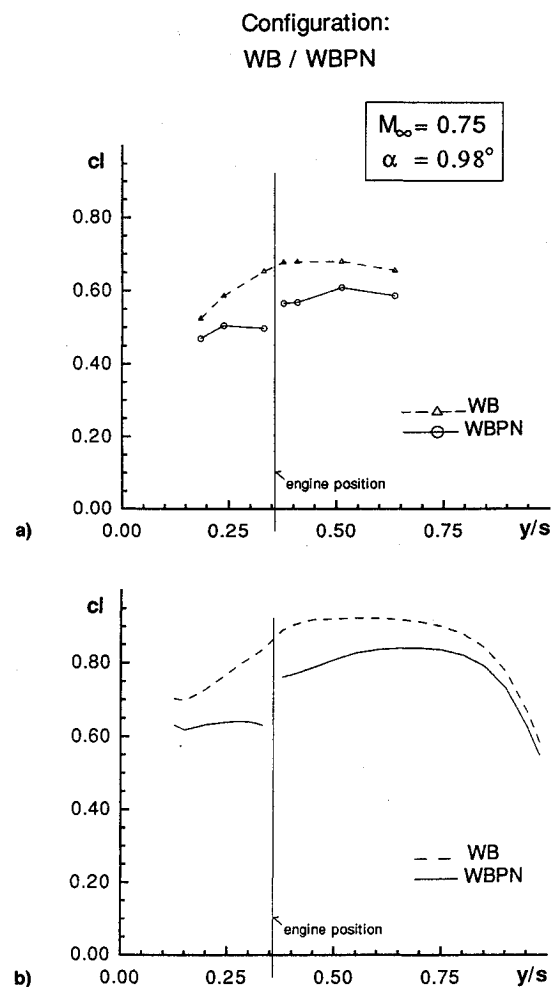


Fig. 7 Spanwise lift distribution with and without nacelles: a) experiment and b) calculation.

sponds to cruise lift of $C_L = 0.5$ for the WBPN configuration in the S2MA wind tunnel.

Local Lift Behavior

Figure 7 shows a comparison of the variation of local lift in spanwise direction for the WB and the WBPN configurations. Figures 7a and 7b display experimental and computational results, respectively. In the case of the experimental results the location of the measuring sections is marked by triangles and circles for WB and WBPN. The configuration with installed nacelle shows a significant loss of lift compared to the clean configuration. At the pylon location, the slope of the local lift curve is discontinuous. This is caused by the fact that on the lower wing surface the pylon separates the flowfield between inboard and outboard side. Both experi-

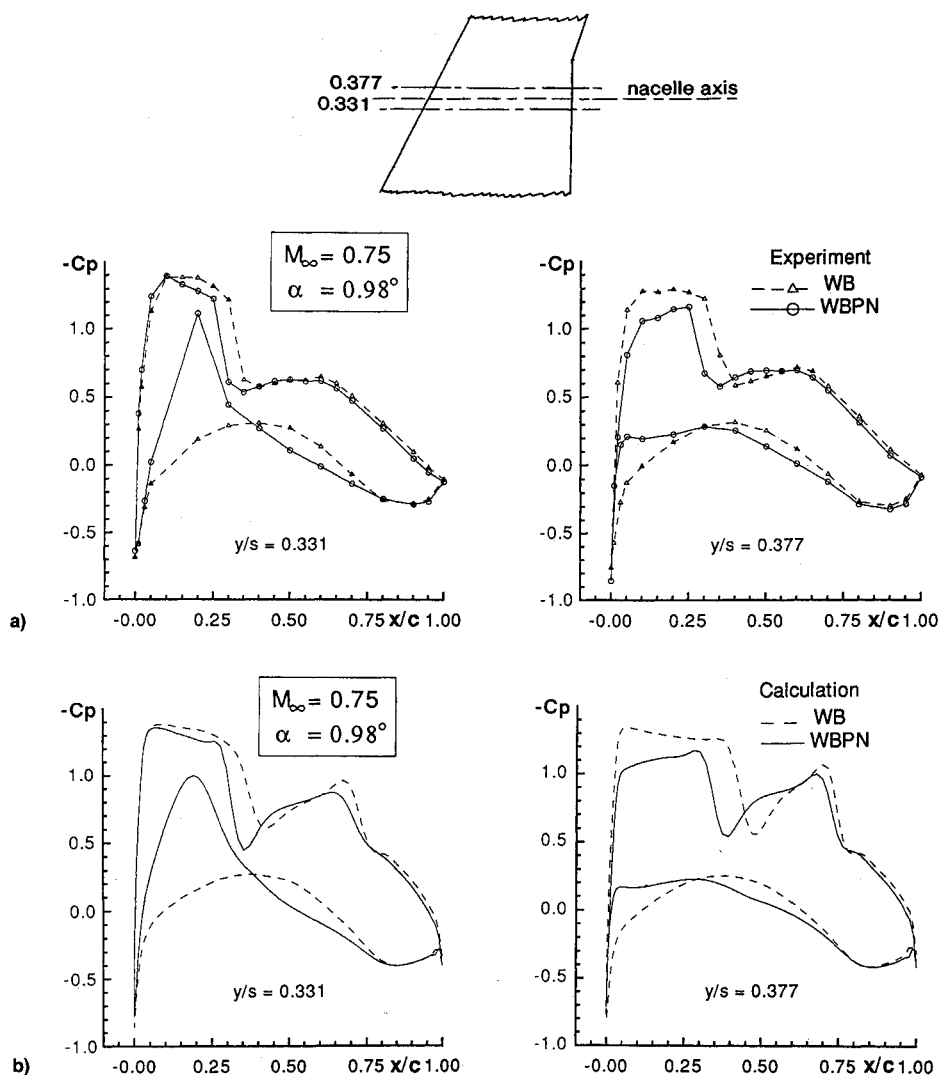


Fig. 8 Sectionwise pressure distributions with and without nacelles: a) experiment and b) calculation.

mental and calculated results exhibit the same qualitative behavior. The calculation, however, overpredicts the local lift of both WB and WBP by roughly 30%. Nevertheless, the amount of lift loss caused by the installation of the nacelle, for both experiment and calculation, is in the range of 10%. This indicates that the calculation is well able to account for the interference effects.

Pressure Distribution on the Wing

To get more detailed information on the interference effects, the flowfield will be analyzed using the wing pressure distribution at spanwise sections closely inboard and outboard of the pylon. Figure 8 displays measured and calculated pressure distributions at the two sections for the clean and the configuration with installed nacelles. Comparing the results of the WB and the WBP configuration one observes that the installation of the nacelles has a significant influence on the flowfield.

Lower Wing Surface

Inboard of the pylon, the main effect is a strong flow acceleration for the WBP configuration with respect to the WB configuration, and a supersonic region is established. The suction peak comes very close to the lowest pressure on the upper wing surface. The supersonic region is terminated by a shock wave. From 35% chord length further downstream, the flow is decelerated compared to the clean configuration.

Outboard of the pylon, for the WBP configuration the flow is significantly accelerated in a small region close to the

leading edge. Further downstream, pressure is only mildly reduced for the WBP configuration. From about 25% chord length the flow around the configuration with installed nacelle is decelerated compared to the clean configuration.

The effects just described are present in the experiments as well as in the computation. The difference in the pressure distribution in- and outboard of the pylon is responsible for the discontinuity found in the lift distribution of Fig. 7. This difference between inboard and outboard pressure distribution is caused by the sweep of the wing. On a swept wing the streamlines of inviscid flow are not straight lines but curved, and therefore the pylon distorts the streamline pattern. Inboard of the pylon the streamlines are compressed, and thus, the flow is accelerated.¹¹ The flow acceleration is aggravated since the nacelle is of long duct type and mounted very closely under the wing. This creates a duct between wing, nacelle, and pylon. Due to the change of cross section in this duct, the flow is even more accelerated.

Due to this acceleration, on the lower wing surface a supersonic region terminated by a shock wave is created. This shock wave and the subsequent separation cause the drag increase of the WBP configuration at low lift, as discussed in the section about lift and drag behavior. Decreasing incidence leads to a further flow acceleration on the lower wing surface, and thus, to a stronger shock wave. Furthermore, the appearance of this shock wave leads to the reduction of the drag rise Mach number, as observed in Fig. 5c.

Outboard of the pylon, the displacement effect of the pylon and the location of the attachment line at the leading edge of

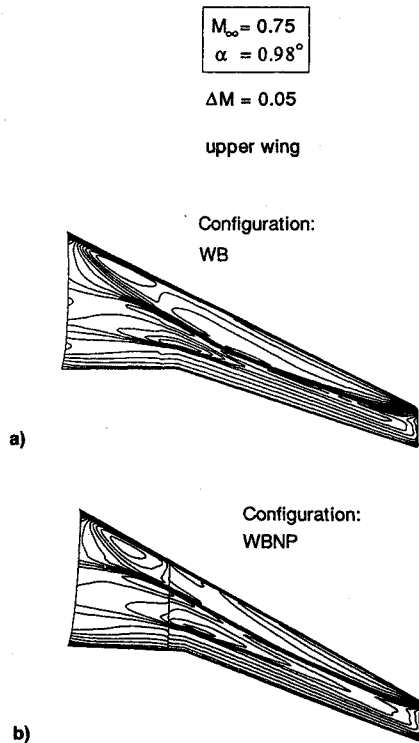


Fig. 9 Computed lines of constant Mach number: a) without nacelles and b) with nacelles.

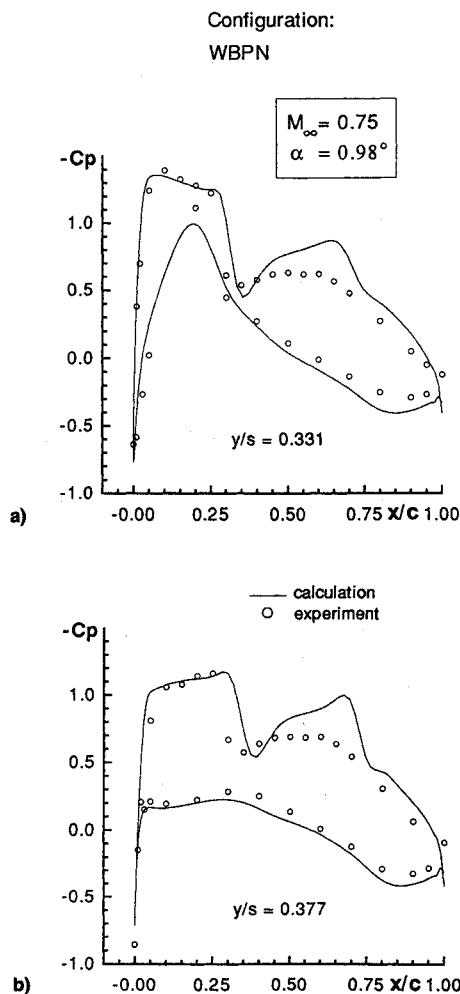


Fig. 10 Experimental and computational wing pressure distribution: a) inboard of pylon and b) outboard of pylon.

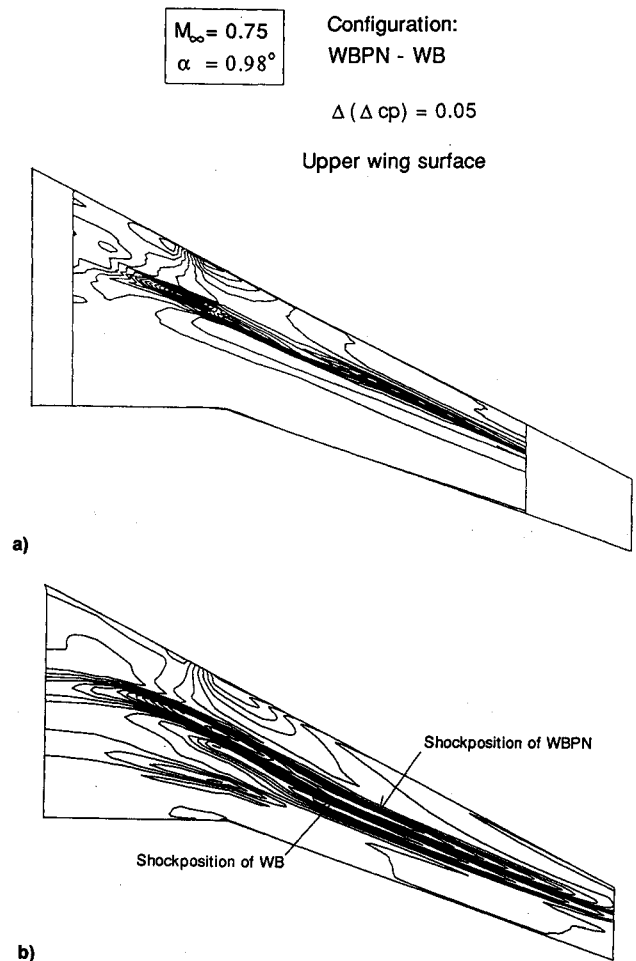


Fig. 11 Pressure difference on upper wing surface: a) experiment and b) calculation.

the pylon cause a strong flow acceleration very close to the wing leading edge. Due to the sweep of the wing, outboard of the pylon streamlines are then widened,¹¹ and no further acceleration as observed inboard takes place.

Upper Wing Surface

On the upper wing surface one observes that the shock has been shifted upstream by the installation of the nacelles. Note that the shift in shock position has been well predicted by the computation.

In order to further investigate the effect of the nacelle on the upper wing surface, Fig. 9 shows lines of constant Mach number for both the clean and the configuration with installed nacelle. Since measurements were only performed at eight spanwise sections, solely computational results are displayed in this figure. The figure shows that the presence of the installed nacelle influences the whole upper surface of the wing. As outlined in Ref. 5, its presence leads to a local reduction in incidence, and therefore, to a forward movement of the shock. The flow on most of the upper surface is supersonic, and therefore this local disturbance is propagated along characteristics. Since the sweep of the wing is 27.1° , which corresponds to the angle of characteristics at $M = 1.12$, the local disturbance may be propagated over the upper surface from the nacelle location up to the wingtip. Thus, the shock moves upstream in this whole region. Due to a channel effect between fuselage and installed nacelle, the change in incidence occurs over the range from fuselage to pylon, and the shock position is also influenced in that region. Therefore, the shock is moved upstream on the complete upper surface.

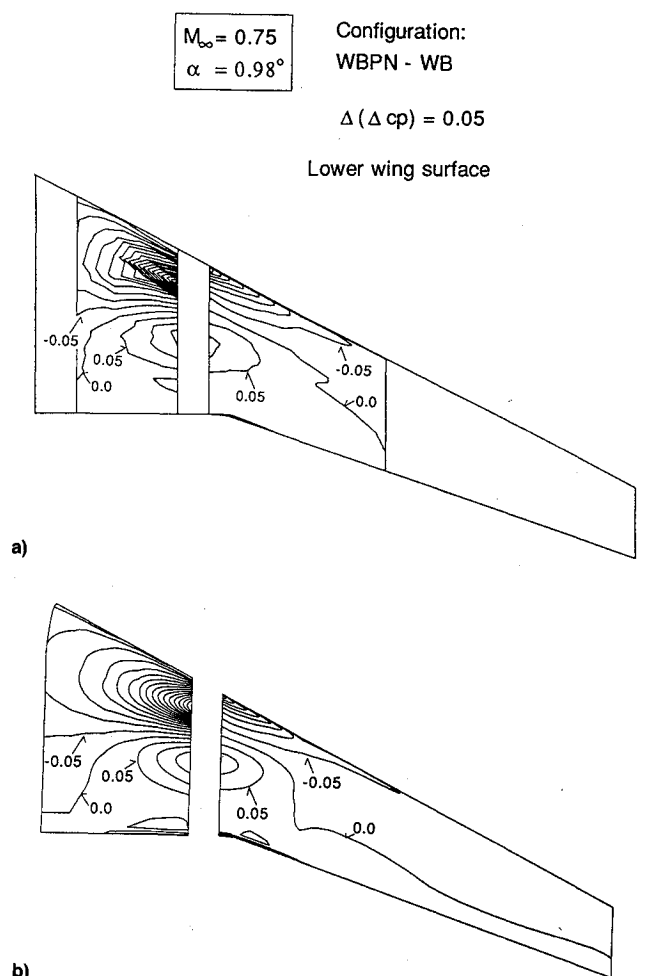


Fig. 12 Pressure difference on lower wing surface: a) experiment and b) calculation.

Comparison of Experiment and Calculation

Figure 10 shows a direct comparison of experiment and calculation for the WBPN configuration in the sections just in- and outboard of the pylon. The differences between calculation and experiment are of the same nature as already discussed when outlining the limitations of the theoretical approach. Therefore, Fig. 10 confirms that the solution of the Euler equations is well suited for the simulation of the interference effects. The suction peak inboard of the pylon on the lower wing surface is as well predicted as the strong acceleration at the wing leading edge outboard of the pylon. Even the deceleration of the flow on the lower surface in the rear part of the wing, resulting from the installation of the nacelle, is accurately predicted by the numerical method.

Display of Pressure Differences

The interference effects discussed above may be very well displayed by visualizing the differences between the pressure distributions of the configuration with installed nacelle (WBPN) and the clean configuration (WB). Positive values of the pressure difference ΔC_p denote deceleration of the flow, and vice versa.

Upper wing surface. Figure 11 shows lines of constant pressure difference between the two configurations on the upper wing surface for both experiment and calculation. In the calculated result the upstream movement of the shock is clearly visible. For the experimental result the two shocks are not that discernible due to the limited amount of pressure taps in the shock region. Both the experiment and the computation further show that the upstream shift of the shock takes place over the whole upper surface.

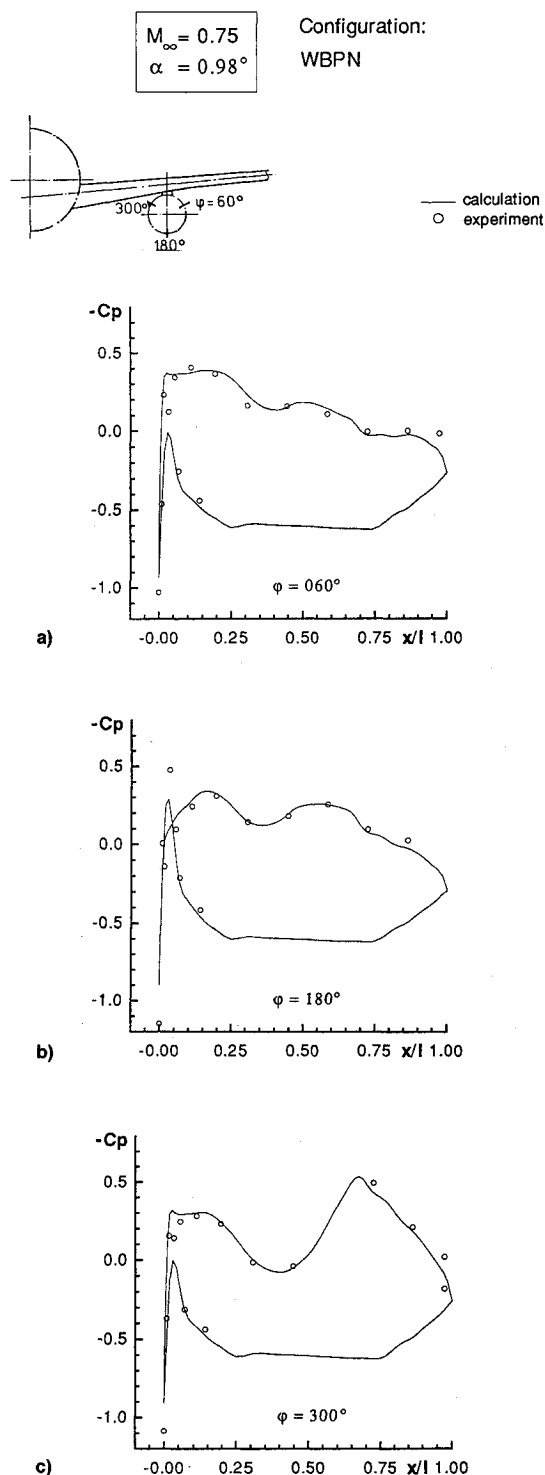


Fig. 13 Experimental and computational nacelle pressure distribution: a) outboard of pylon, b) pylon location, and c) inboard of pylon.

Lower wing surface. Figure 12 displays the pressure differences for the transonic case on the lower wing surface. It is clearly visible that inboard of the pylon the region influenced is by far larger than on the outboard side. The reason for this may be found in the fact that fuselage, or even the symmetry plane, and installed nacelle cause a channel effect at the inboard region of the wing. Thus, acceleration of the flow is not only very intensive closely to the pylon, but remains also noticeable further inboard.

Nacelle Pressure Distribution

Figure 13 shows a comparison of measured and calculated pressure distributions at different sections of the nacelle cor-

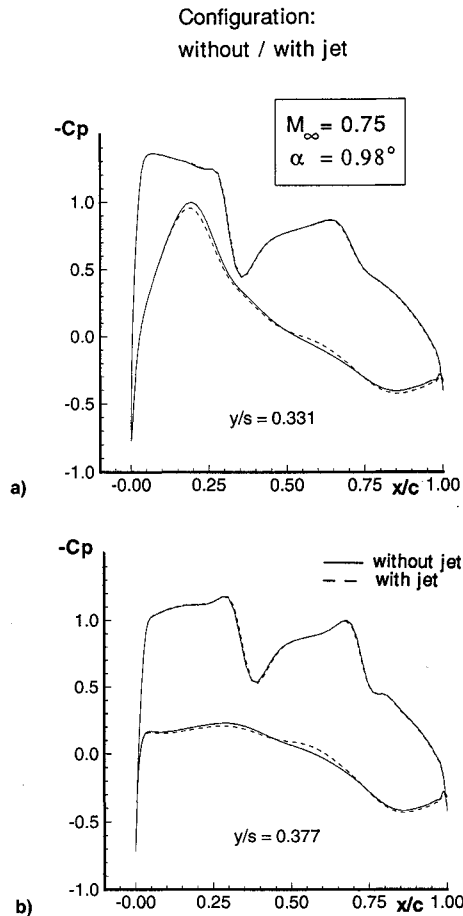


Fig. 14 Computed wing pressure distribution with and without jet: a) inboard of pylon and b) outboard of pylon.

responding to the instrumentation of the model. The nacelle pressure distribution is most severely influenced by interference effects in the section at $\varphi = 300$ deg. The acceleration of the flow in this section is related to the flow acceleration observed inboard of the pylon on the lower wing surface. The agreement between experiment and calculation is very good in all three sections. In Ref. 12 it was already shown that the solution of the Euler equations is well suited for the simulation of the flow around isolated nacelles. This has been explained by the fact that for the flowfield around a nacelle the mass flow through the nacelle is the most important parameter, and the mass flow is not severely influenced by viscous effects.

The solution of the Euler equations accurately models the interference phenomena. The deviation of the pressure distribution in circumferential direction, caused by the influence of the wing, is accurately predicted by the computation. Small deviations between measurement and calculation occur only at the nacelle leading edge. The reason for that may be two-fold. On the one hand the mass flow may not be exactly identical due to viscous effects acting on the internal flow. On the other hand the grid density at the nacelle leading edge may be insufficient to resolve the strong gradients there.

Jet Effect

For the assessment of the interference effects of a real configuration the jet effect has to be considered. Therefore, it is highly desirable to simulate the real physical jet conditions in the experiment as well as in the computation.¹³ However, the simulation of real jet flow requires large efforts. As a first step towards the investigation of jet interference, here the effect of an inviscid jet has been computed. Following Ref. 5, an actuator disk has been used to establish the jet boundary conditions. The pressure ratio at the outflow face was spec-

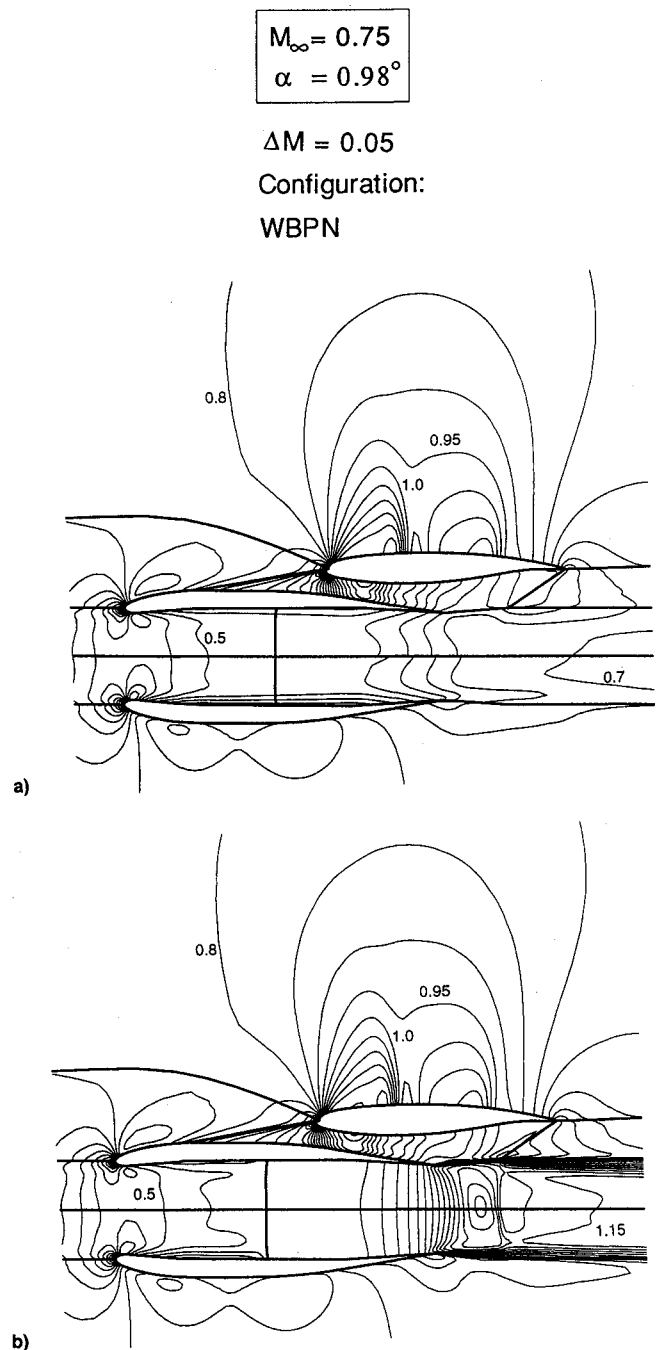


Fig. 15 Mach number distribution at nacelle location: a) without jet and b) with jet.

ified to $p_\infty/p_{\text{tot jet}} = 2.4$. The incoming mass-flow was prescribed with a stream-tube area ratio of $\varepsilon = 0.71$, which corresponds to that of the basic throughflow nacelle.

Figure 14 shows the wing pressure distribution for the configuration with jet and with throughflow nacelle for the sections just in- and outboard of the pylon. Basically, no significant differences are observed between the two cases.

An explanation for this result may be found in Fig. 15, where the flowfield around the two configurations is displayed by lines of constant Mach number in a section through wing and nacelle at the pylon location. In Fig. 15b the jet is clearly visible by the concentration of isolines. Note that in truly inviscid flow, the jet boundaries should be given by contact discontinuities, but the numerical dissipation has a smearing effect. Since the nacelle trailing edge is located at about 50% wing chord length, the inviscid jet has only a very small influence on the interference.

Conclusions

In a cooperative research programme, ONERA and DLR have performed a very detailed analysis of airframe/propulsion integration of a generic twin-engine transport aircraft configuration. The DLR-F6 configuration with long duct throughflow nacelles as propulsion units has been chosen to investigate the interference effects by both experiments and computations.

On the one hand experiments have been carried out in the transonic test section of the S2MA wind tunnel in the ONERA test center at Modane. Overall forces and moments have been measured as well as surface pressure distributions on the wing and the nacelles of the highly instrumented wind-tunnel model.

On the other hand computations on this configuration have been performed using the CEVCATS-code, a multiblock multigrid Euler solver recently developed at DLR and currently applied to complex configurations.

The results of both experiment and computation consistently show substantial interference effects due to the installation of the nacelles on the configuration at cruise Mach number. With respect to the wing-body configuration, total lift decreases at constant incidence, and total drag increases at constant lift due to the installation drag. In addition, the drag rise Mach number for the complete configuration is reduced.

The analysis of the surface pressure distributions on the wing and the nacelle reveals the main features of the interference effects on the flowfield at cruise conditions: the supersonic region on the upper wing surface is reduced over the whole span leading to an upstream movement of the shock. On the lower wing surface inboard of the pylon the flow is accelerated in such a way that a local supersonic region closed by a shock wave appears. In addition, differences in the pressure distributions inboard and outboard of the pylon lead to a discontinuous local lift evolution vs span. As far as the nacelle is concerned, the pressure distribution is also modified by the flow acceleration inboard of the pylon.

Comparisons between measured and calculated pressure distributions demonstrate the capability of the Euler code to correctly predict the interference effects due to the propulsion integration, despite the fact that viscous effects are not included in this approach. In addition, these computations reveal that an inviscid jet does not play an important role in the interference effects on the investigated configuration.

Acknowledgment

The authors wish to thank J. F. Piat from Modane test center for his assistance during the measurements. His work is greatly appreciated.

References

- ¹Mirat, J. J., Perin, R., and Castan, C., "Engine Installation Design for Subsonic Transport Aircraft," *Proceedings of the 17th ICAS Congress* (Stockholm, Sweden), ICAS-AIAA, 1990 (ICAS Paper 90-2.7.3).
- ²Hoheisel, H., Kiock, R., Rossow, C. C., Ronzheimer, A., Baumer, W., and Capdevila, H., "Aspects of Theoretical and Experimental Investigations on Airframe/Engine Integration Problems," *Proceedings of the 17th ICAS Congress* (Stockholm, Sweden), ICAS-AIAA, 1990 (ICAS Paper 90-2.7.4).
- ³Rech, J., "Integration sur Avion des Ensembles Propulsifs Futurs," Colloque AEROPROPULSION 1990, Paris, France, 1990.
- ⁴Godard, J.-L., Jacquotte, O. P., and Gisquet, D., "Analyse Détaillée de l'Interaction Voilure-nacelle d'un Avion de Transport Civil," *Proceedings of the FDP Symposium on Aerodynamic Engine/Airframe Integration for High Performance Aircraft and Missiles* (Fort Worth, TX), AGARD, 1991, pp. 4.1-4.11 (AGARD CP-498).
- ⁵Rossow, C.-C., and Ronzheimer, A., "Investigation of Interference Phenomena of Modern Wing-Mounted High-Bypass-Ratio Engines by the Solution of the Euler Equations," *Proceedings of the FDP Symposium on Aerodynamic Engine/Airframe Integration for High Performance Aircraft and Missiles* (Fort Worth, TX), AGARD, 1991, pp. 5.1-5.11 (AGARD CP-498).
- ⁶Redeker, G., Schmidt, N., and Müller, R., "Design and Experimental Verification of a Transonic Wing for Transport Aircraft," *Proceedings of the FDP Symposium on Subsonic/Transonic Configuration Aerodynamics* (Munich Neubiberg, Germany), AGARD, 1980, pp. 13.1-13.7 (AGARD CP-285).
- ⁷Pierre, M., and Fasso, G., "The Aerodynamic Test Center of Modane-Avrieux," ONERA TN 166E, March 1972.
- ⁸Atkins, H. L., "A Multi-Block Multigrid Method for the Euler and Navier-Stokes Equations for Three-Dimensional Flows," AIAA Paper 91-101, Jan. 1991.
- ⁹Rossow, C.-C., and Ronzheimer, A., "Multi-Block Grid Generation Around Wing-Body-Engine-Pylon Configurations," *Proceedings of the 3rd International Conference on Numerical Grid Generation in Computational Fluid Dynamics and Related Fields* (Barcelona, Spain), 1991, pp. 357-368.
- ¹⁰Wichmann, G., "Ein Verfahren zur Berechnung der Umströmung von Flügel-Rumpf-Konfigurationen unter Berücksichtigung der Tragflügelgrenzschicht," DGLR Rept. 90/06, Sept. 1990.
- ¹¹Küchemann, D., and Weber, J., "Aerodynamics of Propulsion," McGraw-Hill, New York, 1953.
- ¹²Rudnik, R., "Erweiterung eines Dreidimensionalen Euler-Verfahrens zur Berechnung des Strömungsfeldes um Nebenstromtriebwerke mit Fan- und Kernstrahl," DLR-FB 91-13, 1991.
- ¹³Hoheisel, H., Bütefisch, K. A., Lehmann, B., Henke, R., Roscher, H. J., and Sellhorst, U., "The Jet Behaviour of an Actual High-Bypass Engine as Determined by LDA-Measurements in Ground Tests," *Proceedings of the FDP Symposium on Aerodynamic Engine/Airframe Integration for High Performance Aircraft and Missiles* (Fort Worth, TX), AGARD, 1991, pp. 20.1-20.14 (AGARD-CP-498).